

GLOBAL DRAG-INDUCED INSTABILITIES IN PROTOPLANETARY DISKS

MIR ABBAS JALALI

Computational Mechanics Laboratory, Department of Mechanical Engineering
Sharif University of Technology, Azadi Avenue, P.O. Box: 11155-9567, Tehran, Iran

Accepted for publication in the Astrophysical Journal

ABSTRACT

We use the Fokker-Planck equation and model the dispersive dynamics of solid particles in annular protoplanetary disks whose gas component is more massive than the particle phase. We model particle–gas interactions as hard sphere collisions, determine the functional form of diffusion coefficients, and show the existence of two global unstable modes in the particle phase. These modes have spiral patterns with the azimuthal wavenumber $m = 1$ and rotate slowly. We show that in ring-shaped disks, the phase space density of solid particles increases linearly in time towards an accumulation point near the location of pressure maximum, while instabilities grow exponentially. Therefore, planetesimals and planetary cores can be efficiently produced near the peaks of unstable density waves. In this mechanism, particles migrating towards the accumulation point will not participate in the formation of planets, and should eventually form a debris ring like the main asteroid belt or classical Kuiper belt objects. We present the implications of global instabilities to the formation of ice giants and terrestrial planets in the solar system.

Subject headings: methods: numerical, hydrodynamics, instabilities, planets and satellites: formation, planetary systems: protoplanetary disks

1. INTRODUCTION

Protoplanetary disks are multi-phase environments composed of solid particles and molecular gas. The motion of particles is mainly governed by the gravitational forces of the disk material and the central star. Gas molecules feel the pressure gradient as well: for a polytropic isothermal gas, whose density profile monotonically increases towards the central star, the pressure gradient ∇p is always negative. This yields a sub-Keplerian circular velocity and generates headwind on solid particles that move on Keplerian orbits. Solid particles are thus expected to inspiral towards the central star. Although adhesive and electrostatic forces can enhance the clustering of micron-sized particles (Blum & Wurm 2008), centimeter- to meter-size particles seem to inspiral towards (and fall into) the central star sooner than the time scale needed for assembling planetary cores. Therefore, several collective processes like streaming instability (Youdin & Goodman 2005), turbulent vortices induced by Kelvin-Helmholtz instability (Johansen et al. 2006; Bai & Stone 2010a,b) and magnetorotational instability (Johansen et al. 2007, 2011) have been proposed to be responsible for the formation of km-scale planetesimals.

The inspiraling motion of particles, however, does not globally occur in disks with non-monotonic density profiles, which are likely to form through a combination of viscous accretion and photoevaporation by the central star (e.g., Matsuyama et al. 2003). A ring-like disk is the simplest system with non-monotonic density profile. An interesting property of such systems is that ∇p becomes positive in regions where the density profile is rising, and gas molecules move with super-Keplerian velocities. Consequently, solid particles that approximately move on Keplerian orbits are accelerated by gas and migrate outwards. This means that solid particles do

not necessarily fall into the central star and may instead migrate to regions where the pressure is maximum and both the head and tail winds are minimized (Haghighipour & Boss 2003). Migrations of individual particles have been well understood by solving their equations of motion in the presence of gravitational and drag forces, but we do not still know the collective effects of such migrating particles. Can they efficiently produce planetesimals and massive planetary cores?

In this paper, we generalize the analysis of Jalali & Tremaine (2012, hereafter JT12) to disks that include a locally isothermal gas component, and search for global instabilities in the particle phase. Our disks are self-gravitating and the particle phase has non-zero radial velocity dispersion. The dynamics of particles is modeled by the Fokker-Planck equation, and the gas component is assumed to be in a steady-state rotation around the central star. For simplicity, we confine our study to disks with $\Sigma_g/\Sigma_p \gg 1$ where Σ_g and Σ_p are the surface densities of the gas and particle phases, respectively. By this assumption, the background gas component does not respond to the disturbances of the particle phase. We neglect collisions between solid particles, but those between gas molecules and solid particles are taken into account.

We present our simple model of protoplanetary disks in section 2 and derive the circular velocities of solid particles and gas molecules. In section 3, we model the dispersive dynamics of particles in the context of kinetic theory, and utilize a perturbation theory in section 4 to solve the resulting Fokker-Planck equation. In section 5, we apply our theory to planet formation in the solar system, and in section 6 estimate the physical ranges of parameters for which the perturbation solutions are valid. We conclude the paper in section 7 by comparing our findings with previous works. Open problems for future studies are also discussed.

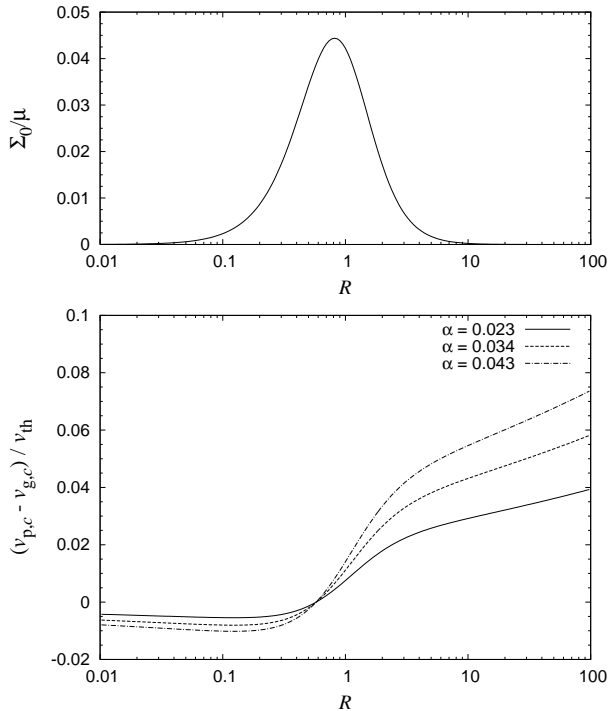


Figure 1. *Top:* Density profile of ring-shaped disks. *Bottom:* Relative circular velocity of particles with respect to gas, normalized to the mean thermal speed of gas molecules. The values of q have been extracted from Table 1.

2. DISK MODEL

We assume a two-phase medium consisting of solid particles and gas molecules, and refer to them by subscripts p and g , respectively. Solid particles are assumed to be monodisperse hard spheres of mass m_p and radius r_p . The gas phase has the molecular mass m_g , and the average radius of gas molecules is r_g . We work with initially axisymmetric disks whose gas component has not streaming motion in the radial direction (no accretion), but particles can move on eccentric orbits. For both the particle and gas phases we use the annular ring model of JT12 whose dimensionless surface density is

$$\Sigma_0(R) = \frac{3\mu}{4\pi} \frac{R^2}{(1+R^2)^{5/2}}, \quad \mu = \frac{M_d}{M_\star}, \quad R = \frac{r}{b}, \quad (1)$$

where $M_d = M_p + M_g$ is the total disk mass, M_\star is the mass of central star, M_p is the mass of particles, M_g is the mass of gas component, b is a length scale, and r is the radial distance to the central star. Top panel in Figure 1 shows the radial profile of Σ_0/μ that peaks at $R = \sqrt{6}/3$. We suppose that the surface densities of the particle and gas phases are proportional to Σ_0 so that $\Sigma_\nu(R) = \bar{M}_\nu \Sigma_0(R)$ with $\nu \equiv p, g$ and $\bar{M}_\nu = M_\nu/M_d$. Defining G as the gravitation constant, the dimensionless total gravitational potential field arising from Σ_0 and the central star becomes

$$V_0(R) = \frac{b\Phi_0}{GM_\star} = -\frac{1}{R} - \frac{\mu}{2} \frac{1+2R^2}{(1+R^2)^{3/2}}, \quad (2)$$

where Φ_0 is the actual potential.

If the gas is locally isothermal, its dimensionless pres-

Table 1
The parameter q for several choices of b in three protoplanetary/planetary systems.

	M_\star/M_\odot	r_\star/r_\odot	T_\star/T_\odot	b (AU)	q
Solar System	1	1	1	3.8	0.023
Solar System	1	1	1	72	0.034
Fomalhaut	1.92	1.82	1.486	243	0.043
AB Aurigae	3.1	2.1	1.3-1.7	69	0.031

sure will be determined from

$$p = c_s^2 \Sigma_g, \quad c_s^2 = \left(\frac{b}{GM_\star} \right) \left(\frac{k_B T_g}{m_g} \right), \quad (3)$$

where c_s is the normalized sound speed, k_B is the Boltzmann constant, and T_g is the absolute gas temperature. In passive disks heated by the stellar radiation (not by accretion), and sufficiently far from the central star, the radial profile of T_g is given by (Armitage 2010, §2.4)

$$T_g = T_\star \left(\frac{2r_\star}{3\pi b} \right)^{3/4} \frac{1}{R^{3/4}}, \quad (4)$$

where T_\star is the effective temperature of the central star and r_\star is its radius. The mean thermal speed of gas molecules is related to the sound speed as $v_{th}^2 = (8/\pi)c_s^2$. We therefore find

$$v_{th} = q R^{-3/8}, \quad q = \left(\frac{8b k_B T_\star}{\pi G M_\star m_g} \right)^{1/2} \left(\frac{2r_\star}{3\pi b} \right)^{3/8}. \quad (5)$$

With m_g being the molecular mass of H_2 , we have computed the value of q and given in Table 1 for several choices of b in the solar system, and around AB Aurigae (Hashimoto et al. 2011) and Fomalhaut. The reason for our special selection of b will be explained in §4.

In the absence of collisions between solid particles and gas molecules, the velocity of solid particles on circular orbits is determined from

$$v_{p,c}^2 = R \frac{dV_0}{dR} = \frac{1}{R} + \frac{\mu}{2} \frac{R^2(2R^2-1)}{(1+R^2)^{5/2}}, \quad (6)$$

and the radial momentum equation for the gas becomes

$$-\Sigma_g \frac{v_{g,c}^2}{R} = -\frac{dp}{dR} - \Sigma_g \frac{dV_0}{dR}, \quad (7)$$

from which we obtain the circular velocity of gas:

$$v_{g,c}^2 = \frac{5\pi}{32} \frac{(1-3R^2)}{(1+R^2)} v_{th}^2 + v_{p,c}^2. \quad (8)$$

The condition $v_{p,c}^2 \geq 0$ implies $\mu \leq 5^{5/2}$, which is satisfied by protoplanetary disks. Bottom panel in Figure 1 illustrates the radial variation of $\Delta v_c = (v_{p,c} - v_{g,c})/v_{th}$ for three values of q . The profile of Δv_c is almost flat for $R \lesssim 0.3$. According to equation (8), the gas streaming velocity exceeds the speed of particles for $R^2 < 1/3$ and generates tailwind on them. This is a remarkable feature of ring-shaped disks, and has interesting implications for the dynamics of solid particles in protoplanetary disks: while particles experience a resistive headwind for $R^2 > 1/3$ and inspiral towards the central star, they are accelerated when $R^2 < 1/3$ and migrate outwards.

Inward and outward migrating particles will then be accumulated near $R^2 \approx 1/3$ where the gas pressure is maximum (see Haghhighipour & Boss 2003). In next sections we show that such migrations are not towards the exact location of pressure maximum if solid particles move on eccentric orbits. Moreover, such migrations are shown to be accompanied by exponentially growing instabilities.

3. EVOLUTIONARY DYNAMICS OF SOLID PARTICLES

The dynamics of particles is described by the phase space distribution function (DF) $f(\mathbf{x}, \mathbf{v}, t) = m_p \mathcal{N}_p(\mathbf{x}, \mathbf{v}, t)$ where \mathcal{N}_p is the number density of particles. The vectors $\mathbf{x} = (x_1, x_2)$ and $\mathbf{v} = (v_1, v_2)$ (both in Cartesian coordinates) are the position and velocity vectors of particles in the disk plane, and t is the time. We utilize the DF (Jalali & Tremaine 2012, §3)

$$f_0 = m_p \mathcal{N}_{p,0} = L^{2K+2} g_K(E), \quad (9)$$

to model the initial distribution of particles, before turning on the collisions between solid particles and gas molecules. Here $L = |\mathbf{x} \times \mathbf{v}|$ and $E = \frac{1}{2} \mathbf{v} \cdot \mathbf{v} + V_0$ are, respectively, the orbital angular momentum and energy of particles per unit mass. There is an invertible, one-to-one and onto map from the (E, L) -space to the space of orbital elements (a, e) where a and e are the orbital semi-major axis and eccentricity, respectively. K is a positive integer that controls the mean eccentricity \bar{e} of the particle disk. The function $g_K(E)$ takes physical (positive) values for $K \geq 2$, and \bar{e} decreases as K is increased. In the limit of $K \rightarrow \infty$ the disk becomes cold with all particles moving on circular orbits.

In this study we ignore particle-particle collisions, and assume that colliding solid particles and gas molecules are hard spheres. The evolution of f is therefore expressed by the Fokker-Planck equation (Binney & Tremaine 2008, §7.4)

$$\begin{aligned} \frac{\partial f}{\partial t} + v_i \frac{\partial f}{\partial x_i} + a_i \frac{\partial f}{\partial v_i} = - \frac{\partial}{\partial v_i} (D[\Delta v_i] f) \\ + \frac{1}{2} \frac{\partial^2}{\partial v_i \partial v_j} (D[\Delta v_i \Delta v_j] f), \end{aligned} \quad (10)$$

where $D[\Delta v_i]$ and $D[\Delta v_i \Delta v_j]$ are diffusion coefficients and a_i are the components of the acceleration vector. In equation (10) and throughout the paper a repeated integer index stands for summation over that index from 1 to 2. The acceleration vector is computed from $\mathbf{a} = -\nabla V = -\nabla[V_0 + V_1(R, \phi, t)]$ where the perturbed potential V_1 is self-consistently calculated from the density disturbance $\Sigma_1(R, \phi, t)$ of particle distribution. Since we have assumed $\Sigma_p \ll \Sigma_g$, the contribution of the gas component to V_1 is neglected.

For local collisions, the diffusion coefficients are evaluated using the procedure of Rosenbluth et al. (1957), but for three dimensional collisions of hard spheres with the cross section $\mathcal{S}_{p,g} = \beta^2/4$ where $\beta = r_p + r_g$. Let us define $\gamma = m_g/(m_p + m_g)$ and denote the absolute velocity of gas molecules by \mathbf{v}' . We obtain

$$D[\Delta v_i] = \frac{\partial h(\mathbf{x}, \mathbf{v}, t)}{\partial v_i}, \quad D[\Delta v_i \Delta v_j] = \frac{\partial^2 g(\mathbf{x}, \mathbf{v}, t)}{\partial v_i \partial v_j}, \quad (11)$$

where the potential functions $h(\mathbf{x}, \mathbf{v}, t)$ and $g(\mathbf{x}, \mathbf{v}, t)$ are

given by the following integrals

$$h = \frac{-\pi\gamma\beta^2}{3} \int \mathcal{N}_g(\mathbf{x}, \mathbf{v}', t) |\mathbf{v} - \mathbf{v}'|^3 d\mathbf{v}', \quad (12)$$

$$g = \frac{\pi\gamma^2\beta^2}{15} \int \mathcal{N}_g(\mathbf{x}, \mathbf{v}', t) |\mathbf{v} - \mathbf{v}'|^5 d\mathbf{v}', \quad (13)$$

and $\mathcal{N}_g(\mathbf{x}, \mathbf{v}', t)$ is the number density of gas molecules in the phase space. In deriving equations (12) and (13) we have assumed three-dimensional scattering of gas molecules by solid objects whose motion is confined to the disk plane. Therefore, the velocity vector of gas molecules is $\mathbf{v}' = (v'_1, v'_2, v'_3)$ where v'_3 is the velocity component perpendicular to the disk plane. Defining

$$[\Sigma_p, \Sigma_p \bar{v}_i, \Sigma_p \overline{v_i v_j}] = \int [1, v_i, v_i v_j] f d\mathbf{v}, \quad (14)$$

the elements of the stress tensor are determined as $\tau_{ij} = \Sigma_p (\overline{v_i v_j} - \bar{v}_i \bar{v}_j)$. The macroscopic quantities Σ_p , \bar{v}_i and τ_{ij} are functions of \mathbf{x} and t , and the second term on the right-hand side of equation (10) integrates to zero up to the first-order moment equations. Collisional terms involving $g(\mathbf{x}, \mathbf{v}, t)$ correspond to random motions, and contribute to the evolutionary equations of τ_{ij} (second-order moments of the Fokker-Planck equation). We neglect them in the present study because the mass ratio of gas molecules to solid particles is small, $m_g/m_p \ll 1$, which implies $g/h \sim \mathcal{O}(m_g/m_p)$. The Fokker-Planck equation can therefore be reduced to

$$\frac{\partial f}{\partial t} + \frac{\partial}{\partial x_i} (\dot{x}_i f) + \frac{\partial}{\partial v_i} (\dot{v}_i f) = 0, \quad (15)$$

with the dimensionless motion equations

$$\dot{x}_i = v_i, \quad \dot{v}_i = -\frac{\partial V}{\partial x_i} + \frac{b^2}{GM_\star} D[\Delta v_i]. \quad (16)$$

Differentiating (12) with respect to v_i gives

$$D[\Delta v_i] = -\pi\gamma\beta^2 \int \mathcal{N}_g(\mathbf{x}, \mathbf{v}', t) |\mathbf{v} - \mathbf{v}'| (v_i - v'_i) d\mathbf{v}'. \quad (17)$$

Evaluating this integral requires the explicit form of \mathcal{N}_g . Nonetheless, such details are not necessary if we make some further simplifying assumptions: Let $(\mathbf{e}_R, \mathbf{e}_\phi)$ be unit base vectors in the polar coordinates (R, ϕ) . For $e \ll 1$, the velocities of particles and gas molecules will be approximated as

$$\mathbf{v} \sim v_{p,c} \mathbf{e}_\phi + \mathcal{O}(eR\Omega), \quad \mathbf{v}' \sim v_{g,c} \mathbf{e}_\phi + \mathcal{O}(v_{th}), \quad (18)$$

where $\Omega = R^{-3/2} + \mathcal{O}(\mu)$ is the orbital frequency of particles. We think of disks with $v_{th} < v_{p,c}, v_{g,c}$ over $0.03 \lesssim R \lesssim 10$ (cf. Figure 1) to guarantee the existence of bound orbits, and avoid gas dispersal through photoevaporation. The mean eccentricity corresponding to (9) is almost constant over the entire disk space (see JT12), and it is given by $\bar{e} = [\pi/(4K+2)]^{1/2} + \mathcal{O}(\mu)$. For $q \sim \mathcal{O}(10^{-2})$, which corresponds to protoplanetary disks around solar-type stars, and for $K \leq 29$ experimented in JT12, one has

$$\bar{e} \gg \frac{v_{th}}{R\Omega} = qR^{1/8} + \mathcal{O}(\mu), \quad 0.03 \leq R \leq 10. \quad (19)$$

From (8), (18) and (19) we conclude that the bulk of particles move with supersonic speeds with respect to the gas stream, and they satisfy $|\mathbf{v} - \mathbf{v}'| \approx eR\Omega$. The integral in (17) is thus approximated by

$$\frac{b^2}{GM_\star} D[\Delta v_i] \approx -\xi_0 eR\Omega \rho_g (v_i - U_i), \quad (20)$$

$$\xi_0 = \pi \left(\frac{M_\star}{m_p} \right) \left(\frac{r_p}{b} \right)^2, \quad (21)$$

where $\rho_g = \Sigma_g(R)\delta(z)$ and $U_i(\mathbf{x}, t) = \bar{v}'_i$ are the spatial density and streaming velocity components of the gas phase, respectively. Here $\delta(z)$ is Dirac's delta function and z measures the height above the disk mid-plane. The gas density and velocity components have been normalized to M_\star/b^3 and $[GM_\star/b]^{1/2}$, respectively. Equation (20) is equivalent to the drag force expression of Kwok (1975) in supersonic regimes. Assuming that the mass of each particle is computed from $m_p = (4/3)\pi\rho_s r_p^3$, with ρ_s being the typical density of rocky material, one finds $\xi_0 \propto 1/r_p$. With $\xi_0 = (M_\star/m_p)(r_p/b)$ the scattering of gas molecules takes place in the disk plane and the cross section $\mathcal{S}_{p,g}$ becomes a line of the length $r_p + r_g$. We are not interested in this extreme unphysical case.

For near-circular orbits with $e \rightarrow 0$, one obtains $|\mathbf{v} - \mathbf{v}'| \approx v_{\text{th}}$ and $D[\Delta v_i]$ transforms to the well-known form of Epstein drag:

$$\frac{b^2}{GM_\star} D[\Delta v_i] \approx -\xi_0 v_{\text{th}} \rho_g (v_i - U_i). \quad (22)$$

During our numerical computations we use equation (20) if $e v_{p,c} > v_{\text{th}}$ and apply (22) otherwise. A factor $4/3$ is missing on the right hand side of equation (22). It can be recovered through assuming a Maxwell-Boltzmann distribution in the velocity space for \mathcal{N}_g , and exactly performing the integral in (17). Nonetheless, the missing factor is unimportant in our computations, for we will vary ξ_0 to explore the influence of drag force on the disk evolution, and one may suppose that any constant factor have already been included in ξ_0 . To compute diffusion coefficients numerically, we soften Dirac's delta function using its normal distribution representation:

$$\rho_g = \frac{\Sigma_g(R)}{\sqrt{2\pi}h} e^{-z^2/2h^2}, \quad \int_{-\infty}^{+\infty} \rho_g dz = \Sigma_g, \quad (23)$$

where $h \ll 1$ is the dimensionless scale-height of the disk and can be a function of R . The three dimensional structure and evolution of circumstellar disks have not been modeled in this study; we thus work with a constant h and set

$$\xi_0 \rho_g = \xi \Sigma_g, \quad \xi = \frac{\xi_0}{\sqrt{2\pi}h}, \quad (24)$$

in the disk mid-plane where the Fokker-Planck equation governs the evolution of the particle phase.

Solving (15) in a four-dimensional phase space, with particle motions confined to the disk plane, is facilitated by utilizing the angle variables $\mathbf{w} = (w_1, w_2)$ and their conjugate actions $\mathbf{J} = (J_1, J_2)$. We follow JT12 and set J_1 and J_2 to the radial action J_R and the orbital angular momentum $J_\phi = Rv_\phi$, respectively. In the (\mathbf{w}, \mathbf{J}) -space,

the motion equations (16) become

$$\dot{w}_i = \frac{\partial \mathcal{H}}{\partial J_i} - F_{J_i}, \quad \dot{J}_i = -\frac{\partial \mathcal{H}}{\partial w_i} + F_{w_i}, \quad i = 1, 2, \quad (25)$$

where $\mathcal{H} = \frac{1}{2}\mathbf{v} \cdot \mathbf{v} + V(\mathbf{x}, t)$ is the Hamiltonian function, and the generalized forces F_{J_i} and F_{w_i} are determined using the virtual work of nonconservative forces:

$$F_{w_i} \delta w_i + F_{J_i} \delta J_i = \frac{b^2}{GM_\star} D[\Delta v_i] \cdot \delta x_i, \quad (26)$$

with δ being the variational operator. In Appendix A we explain the procedure of calculating $F_{w_i}(\mathbf{J}, w_1)$ and $F_{J_i}(\mathbf{J}, w_1)$. They are real harmonic functions of w_1 and are smooth in the \mathbf{J} -space. We now write equation (15) in the angle-action space:

$$\frac{\partial f}{\partial t} + [f, \mathcal{H}] + \mathcal{D}_F f = 0, \quad (27)$$

where $[\dots]$ denotes the Poisson bracket over the (\mathbf{w}, \mathbf{J}) -space and the *collision operator* \mathcal{D}_F is defined by

$$\mathcal{D}_F = \frac{\partial F_{w_i}}{\partial J_i} - \frac{\partial F_{J_i}}{\partial w_i} + F_{w_i} \frac{\partial}{\partial J_i} - F_{J_i} \frac{\partial}{\partial w_i}. \quad (28)$$

4. UNSTABLE MODES

We seek solutions of the form $f = f_0(\mathbf{J}) + f_1(\mathbf{w}, \mathbf{J}, t)$ for equation (27) so that $|f_1| \ll |f_0|$. The Hamiltonian corresponding to f will become $\mathcal{H} = \mathcal{H}_0 + V_1$ where the perturbed potential V_1 (self-consistently arising from f_1) and $\mathcal{H}_0 = \frac{1}{2}\mathbf{v} \cdot \mathbf{v} + V_0(R)$ are expressed in the angle-action space (Jalali 2010, §2). f_1 is obtained by solving the perturbed Fokker-Planck equation:

$$\frac{\partial f_1}{\partial t} + [f_1, \mathcal{H}_0] + [f_0, V_1] + \mathcal{D}_F f_1 = -\mathcal{D}_F f_0, \quad (29)$$

which is a non-homogenous partial differential equation.

4.1. Secular Migrations

The particular solution of (29) is a radial drift of the form $f_d(\mathbf{J}, w_1, t)$. For the small disturbances $|f_d| \ll |f_0|$, we can ignore $\mathcal{D}_F f_d$ against $\mathcal{D}_F f_0$ and write

$$\frac{\partial f_d}{\partial t} + [f_d, \mathcal{H}_0] + [f_0, V_d] = -\mathcal{D}_F f_0, \quad (30)$$

where the left hand side is the linear approximation of the total derivative df_d/dt , and the potential V_d corresponds to f_d . From the definition of \mathcal{D}_F and equations (A8)–(A10), we arrive at

$$-\mathcal{D}_F f_0 = \sum_{l=-\infty}^{+\infty} S_l(\mathbf{J}) e^{ilw_R}, \quad (31)$$

whose $l \neq 0$ terms lead to particular periodic solutions $f_d(\mathbf{J}, w_1) = f_d(\mathbf{J}, w_1 + 2\pi)$. However, the dominant collisional term

$$S_0(\mathbf{J}) = -\frac{\partial}{\partial J_i} (f_0 F_{w_i}^0), \quad (32)$$

$$F_{w_1}^0 = \sum_{l=-\infty}^{+\infty} l Q_{R,l} \xi_{(-l)} + \sum_{l,l'=-\infty}^{+\infty} l \eta_l \eta_{(-l')} Q_{\phi,(-l-l')},$$

$$F_{w_2}^0 = Q_{\phi,0}.$$

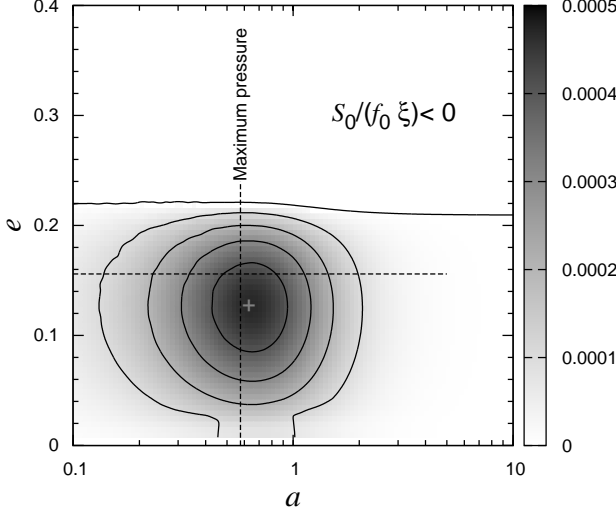


Figure 2. Isocontours of the collisional term $S_0/(f_0\xi)$ in the space of orbital elements. Horizontal dashed line corresponds to the mean eccentricity $\bar{e} = 0.156$ of particle orbits in the initial model. Mass parameters have been set to $\mu = 0.04$ and $\mu_p = 1/8$. Particles migrate linear in time towards the accumulation point $(a_0, e_0) \approx (0.63, 0.128)$ shown by a cross. Contour lines mark the levels 0.0 to 4×10^{-4} with steps of 10^{-4} . Note the logarithmic scale of the a -axis.

results in a *secular* drift $f_d \sim S_0 t$ in the phase space: the DF of particles linearly increases in time if their actions satisfy $S_0(\mathbf{J}) > 0$, and it decreases for $S_0(\mathbf{J}) < 0$. Such drag-induced migrations can accumulate particles in regions where $S_0(\mathbf{J})$ has a positive local maximum. Since S_0 (and therefore df_d/dt) depends on the initial DF, it is useful to normalize it to f_0 and investigate the relative variation of particle distribution in the (a, e) -space.

For a model with $K = 29$ and $q = 0.034$, we have plotted the contours of $S_0/(f_0\xi)$ in Figure 2 for mass parameters $\mu = 0.04$ and $\mu_p = M_p/M_g = 1/8$. The mean eccentricity of particle orbits of this model is $\bar{e} = 0.156$. It is seen that $S_0/(f_0\xi)$ is negative for eccentric orbits with $e \gtrsim 0.22$ and the population of those orbits is falling in time. Meanwhile, the number of particles increases towards an *accumulation point* at $(a_0, e_0) \approx (0.63, 0.128)$. The eccentricity of this accumulation point is less than the mean eccentricity of the initial model, and its semi-major axis is very close to $R = 0.577$ where the gas pressure is maximum. The local maximum of $S_0/(f_0\xi)$ in the (a, e) -space is reminiscent of the distribution of asteroids between Mars and Jupiter with the mean orbital eccentricity ≈ 0.14 , and classical Kuiper belt objects (KBOs) with $\bar{e}_{\text{KBO}} \approx 0.1$. The mean semi-major axis of classical KBOs is $\bar{a}_{\text{KBO}} \approx 45$ AU. If we assume that they are remnants of planet formation that reside at the accumulation point, the length scale b of our annular disk model reads $b = \bar{a}_{\text{KBO}}/a_0 \approx 71.43$ AU, which gives $q \approx 0.034$ used in computations of Figure 2 (see also Table 1). Moreover, for the asteroids between Mars and Jupiter the semi-major axis ranges from $a_{\text{AST}} \approx 2.1$ to 3.3 AU. The most populous group of these asteroids has a mean semi-major axis of $\bar{a}_{\text{AST}} \approx 2.4$ AU. The second plausible length scale of our model is therefore $b = \bar{a}_{\text{AST}}/a_0 \approx 3.81$ AU that corresponds to $q \approx 0.023$. Decreasing μ and μ_p does not considerably change the pattern of $S_0/(f_0\xi)$, but proportionally decreases its maximum value at the accumulation point.

4.2. Exponentially Growing Instabilities

We now search for non-axisymmetric homogeneous solutions of equation (29) that depend on (w_1, w_2, t) , and satisfy

$$\frac{\partial f_1}{\partial t} + [f_1, \mathcal{H}_0] + [f_0, V_1] + \mathcal{D}_F f_1 = 0. \quad (33)$$

We consider unsteady DFs of the form (JT12, §6)

$$f_1 = \tilde{f}_1(\mathbf{J}) e^{-i\omega t + im(w_2 - w_1)}, \quad \omega = \omega_r + is, \quad (34)$$

that corresponds to a slowly rotating density wave with the azimuthal wavenumber m :

$$\Sigma_1 = \text{Re} \int f_1 d\mathbf{v} = e^{st} A(R) \cos[m\phi - \omega_r t + \vartheta(R)]. \quad (35)$$

Here ω_r/m and s are the pattern speed and growth/decay rate of density perturbations, respectively. The radial profiles of the wave amplitude $A(R)$ and phase angle $\vartheta(R)$ are time-invariant in the linear regime, and ϑ vanishes for stable waves with $s = 0$. The perturbed potential

$$V_1 = \tilde{V}_1(\mathbf{J}) e^{-i\omega t + im(w_2 - w_1)}, \quad (36)$$

and density Σ_1 are related through Poisson's integral. In this paper we work with lopsided $m = 1$ waves, which accelerate the central star. Therefore, the reference frame attached to the central star is not inertial, and we include the indirect gravitational potential (see JT12) in our formulation.

Substituting from (34) and (36) into (33) yields the following linear eigenvalue problem for ω and its associated eigenfunction \tilde{f}_1 :

$$\left[\omega - \varpi + i \left(\frac{\partial F_{w_i}}{\partial J_i} + F_{J_2} - F_{J_1} \right) \right] e^{-iw_1} \tilde{f}_1 + ie^{-iw_1} \frac{\partial \tilde{f}_1}{\partial J_i} F_{w_i} + \left(\frac{\partial f_0}{\partial J_2} - \frac{\partial f_0}{\partial J_1} \right) e^{-iw_1} \tilde{V}_1 = 0, \quad (37)$$

where $\varpi(\mathbf{J}) = \Omega_2(\mathbf{J}) - \Omega_1(\mathbf{J})$ is the precession frequency of particle orbits. The orbital frequencies $\Omega_i(\mathbf{J}) = \partial \mathcal{H}_0 / \partial J_i$ ($i = 1, 2$) are determined in the unperturbed state. For nearly circular orbits one finds (JT12)

$$\varpi_c(R) = \frac{3\mu R^{3/2}(1 - 4R^2)}{4(1 + R^2)^{7/2}} + \mathcal{O}(\mu^2), \quad (38)$$

which has the maximum value $\varpi_{\text{max}} = 0.05861\mu$ at $R = 0.2859$. We utilize the finite element method of Jalali (2010) and JT12, and compute the eigenfrequency spectrum of (37) for a model with $K = 29$ and $q = 0.034$. We vary μ , μ_p and ξ to investigate the effects of particle size and mass fraction on the development of density waves. Our finite element model has $N = 200$ ring elements whose radial nodes are located at $R_n = 10^{(4n - 2N - 4)/(N+1)}$ for $n = 1, 2, \dots, N$. Using this mesh, eigenfrequencies are calculated with a relative accuracy $\leq 0.5\%$.

In the absence of gas drag, $\xi = 0$, and for $1/32 \leq \mu_p \leq 1/8$, the spectrum contains two stable slow modes, which are labelled by A_1 (fundamental mode) and A_2 (secondary mode). The pattern speeds of these modes satisfy the inequality $\omega_r \gtrsim \varpi_{\text{max}}$. All other modes are

Table 2
 Pattern speeds and growth rates of slow modes A_1 and A_2 versus ξ . In all models we have set $K = 29$ and $q = 0.034$.

model	model parameters					Mode A_1		Mode A_2	
	μ	μ_p	$\varpi_{\min} \times 10^3$	$\varpi_{\max} \times 10^3$	ξ	ω_r/ϖ_{\max}	$s \times 10^5$	ω_r/ϖ_{\max}	$s \times 10^5$
1	0.04	1/8	-8.239	2.344	0	1.105	0	1.053	0
2	0.04	1/8	-8.239	2.344	0.10	1.105	1.719	1.053	1.908
3	0.04	1/8	-8.239	2.344	0.20	1.106	3.428	1.052	3.821
4	0.04	1/8	-8.239	2.344	0.40	1.110	6.777	1.051	7.638
5	0.04	1/16	-8.239	2.344	0	1.034	0	0.9995	0
6	0.04	1/16	-8.239	2.344	0.10	1.034	1.908	0.9997	1.848
7	0.04	1/16	-8.239	2.344	0.20	1.036	3.787	1.000	3.516
8	0.04	1/16	-8.239	2.344	0.40	1.040	7.386	–	–
9	0.02	1/16	-4.137	1.172	0	1.034	0	0.9994	0
10	0.02	1/16	-4.137	1.172	0.10	1.034	0.954	0.9995	0.924
11	0.02	1/16	-4.137	1.172	0.20	1.035	1.893	1.000	1.758
12	0.02	1/16	-4.137	1.172	0.40	1.040	3.693	–	–
13	0.01	1/32	-2.073	0.586	0	0.998	0	0.977	0
14	0.01	1/32	-2.073	0.586	0.10	0.999	0.494	–	–
15	0.01	1/32	-2.073	0.586	0.20	1.001	0.947	–	–
16	0.01	1/32	-2.073	0.586	0.40	1.005	1.756	–	–

singular and form a continuum over the range $\varpi_{\min} < \omega_r < \varpi_{\max}$. The minimum and maximum precession frequencies, ϖ_{\min} and ϖ_{\max} , occur at the circular orbit boundary of the action space with $J_1 = 0$, and $\varpi(\mathbf{J})$ vanishes for radial orbits. Singular modes are associated with the inner Lindblad resonance $\varpi(\mathbf{J}) - \omega_r = 0$ and they can engage both circular and non-circular orbits. Table 2 shows the variation of ϖ_{\min} and ϖ_{\max} in terms of μ and μ_p .

By setting $\xi > 0$ and turning on the gas drag, all singular and long-wavelength modes become unstable. The pattern speeds and growth rates of modes A_1 and A_2 have been reported in Table 2 for 16 different models whose particle and gas phases are Toomre stable. It is seen that ω_r/ϖ_{\max} is a function of μ_p , and s is an almost linear function of $\xi \bar{M}_g = \xi \mu / (1 + \mu_p)$. Gas drag has not a notable contribution to the pattern speeds of modes and it only controls the growth rate. Figure 3 displays the perturbed density patterns of stable model 1 and unstable model 4. Except in model with $\mu_p = 1/8$, mode A_1 always rotates and grows faster than mode A_2 . Comparing the modal content of our $\xi = 0$ disks with the results of JT12 (see their Figure 4) shows that short-wavelength slow modes have been disappeared by setting $M_p < M_d$ and the pattern speeds of the modes with the longest wavelengths have approached to ϖ_{\max}^+ . This is very similar to the behavior of disk galaxies: increasing the mass of dark matter halo stabilizes tightly wound spiral modes and only modes with the longest wavelengths, especially the bar mode, survive (Jalali 2007).

Figure 4 demonstrates the amplitude function $A(R)$ for several models. It is seen that by increasing ξ the local minimum between two density maxima increases. This is because of the enhanced spirality that smoothly connects density bumps. The local minimum is exactly equal to zero in models with $\xi = 0$ and corresponds to a node of stable oscillatory waves. Varying μ does not change the mode shape (this had already been pointed out by JT12), but decreasing μ_p shortens the wavelength of both modes

A_1 and A_2 . Variation of q has a negligible effect on the eigenmodes. Our experiments show that reducing q from 0.034 to 0.023 changes the eigenfrequencies by $\approx 0.2\%$.

For discrete slow modes, resonant cavities become smaller as μ_p falls off and mode A_2 disappears: mode A_2 has hardly managed to exist in model 13, which is stable. Nonexistence of mode A_2 in models with $\mu_p = 1/16$ and $\xi \gtrsim 0.2$, shows that the development of unstable wave packets is allowed only for $\xi < \xi_{\text{cr}}$ where the critical drag parameter ξ_{cr} depends on both μ and μ_p . Also note the nonexistence of unstable secondary modes in models with $\mu_p = 1/32$. We have a simple physical explanation for the existence of a critical drag parameter: slow modes are supported by the precession of orbits and the leading or trailing nature of developing unstable spiral patterns can be estimated using $d\varpi_c/dR$, which switches sign at $R = 0.2859$. Spiral patterns will be trailing if $d\varpi_c/dR < 0$ and leading otherwise (cf. Binney & Tremaine 2008, §6.1.3). In the region occupied by the central wave packet of mode A_2 (see Figure 4), and when the mode is unstable, the quantity $d\varpi_c/dR$ can take both negative and positive values and that wave packet will be sheared. Larger the value of ξ higher the imposed shearing. The wave packet can thus resist disruption only for small deformations corresponding to $\xi < \xi_{\text{cr}}$. It is evident from Figure 3 that the inner wave packet of mode A_2 leads its stable counterpart because it lies in the region with $d\varpi_c/dR < 0$. The opposite phenomenon is happening for the outer wave packet.

Only mode A_1 can marginally tolerate $\omega_r/\varpi_{\max} \lesssim 1$ and $\xi > 0$ because the local minimum of $A(R)$ is located near the maximum of ϖ_c , and its two main wave packets lie in regions where $d\varpi_c/dR$ has a definite sign. Moreover, its resonant zone is large enough to trap non-circular orbits with $\varpi(\mathbf{J}) < \varpi_{\max}$. The number of slow modes also depends on the mean eccentricity of particle orbits. Our numerical experiments with $\mu_p = 1/8$ show that mode A_2 completely disappears as its pattern speed drops below ϖ_{\max} by increasing \bar{e} .

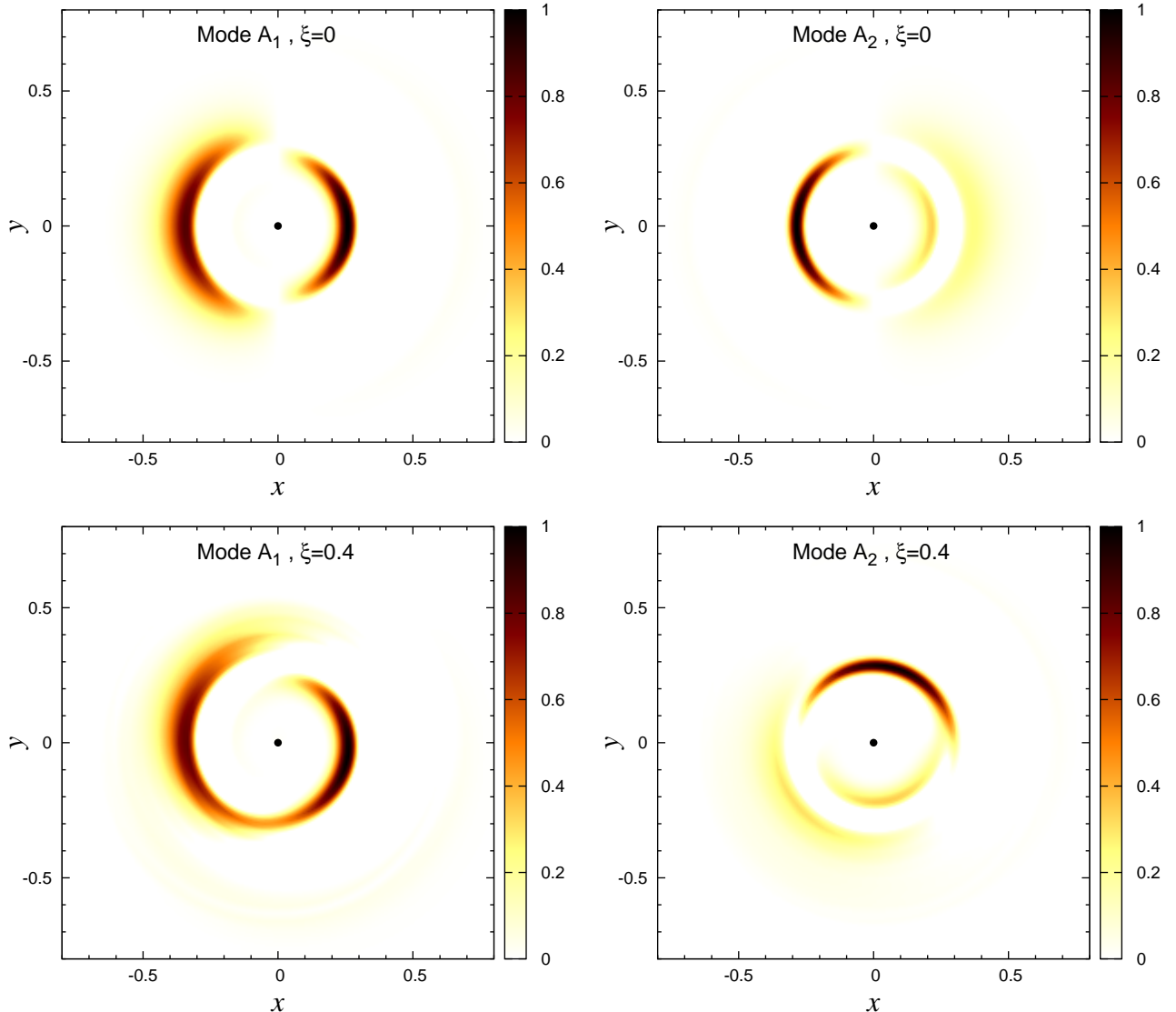


Figure 3. Mode shapes of global stable (*top*) and unstable (*bottom*) density waves of the particle phase in a protoplanetary disk with $\mu = 0.04$, $M_p/M_g = 1/8$ and $\bar{e} = 0.156$. Contour plots show the positive parts of the perturbed density Σ_1 at $t = 0$. In all cases, density waves rotate counterclockwise and their corresponding pattern speeds are given in Table 2. The outer density bump of unstable mode A_1 is a trailing spiral. The inner and outer wave packets of unstable mode A_2 lead and trail their stable counterparts, respectively. Solid circle shows the location of the central star.

Except for $\xi = 0$, $f_0(\mathcal{J})$ is not an equilibrium DF and it is regarded as the initial condition for the perturbed Fokker-Planck equation. It is hard to imagine an equilibrium state at early epochs of protoplanetary disks when most ingredients of planet formation are transported due to dissipative forces. There is indeed a competition between the homogenous and particular solutions of equation (29) and the relative magnitude of s with respect to S_0/f_0 decides which process wins. According to Figures 2 and 3, near the major peaks of modes A_1 and A_2 we have $S_0/f_0 \approx 2 \times 10^{-4}\xi$, which has exactly the same order of magnitude of s for unstable $\mu_p = 1/8$ models of Table 2. Drag-induced instabilities that grow proportional to e^{st} can therefore overwhelm secular migrations, consume most solid particle reserve of the disk within $R < a_0$, and rapidly form bigger objects. Near the accumulation point, the amplitude of unstable density waves diminishes significantly, but since secular migration is a very slow process (linear in time), particles are expected

to form only a debris ring as the gas is depleted at the later stages of disk evolution. A small fraction of solid particles will eventually live in the vicinity of the accumulation point and majority of them are transported through spiral arms to unstable regions.

5. APPLICATIONS TO THE SOLAR SYSTEM

To this end, we discuss the implications of global drag-induced instabilities to planet formation in the solar system. We use the amplitude functions of modes in model 1 because their profiles does not change significantly by varying the mass parameters and ξ (see Figure 4).

According to simulations of circumstellar disks, viscous accretion, photoevaporation and stellar winds create a gap structure near the gravitational radius (Matsuyama et al. 2003), and the disk is split to two annuli. For the solar nebula, the gravitational radius is between the orbits of Saturn and Uranus (Shu et al. 1993), and therefore, the outer ring of the solar system would contain ice giants and KBOs. If we suppose that

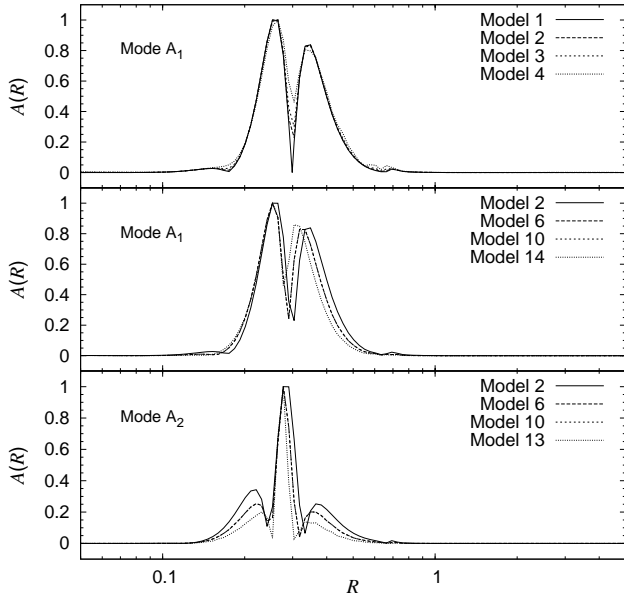


Figure 4. Variation of the amplitude profile $A(R)$ of modes A_1 and A_2 in models with different mass parameters and drag coefficients. See Table 2 for the specifications of the models. The difference between models 6 and 10 is indistinguishable in the plots. The R -axis is in logarithmic scale.

classical KBOs are the debris material near the accumulation point, our ring-like disks and their modal content can be fit to the structure of the outer solar system by assuming $b = \bar{a}_{\text{KBO}}/a_0 = 71.43$ AU (top panel in Figure 5). Interestingly, the semi-major axis of Uranus and Neptune is clearly associated with the outer bump. If we assume that both planets were formed exactly at the peaks of mode A_1 , Uranus and Neptune should have migrated outwards for about 1.5 and 6 AU, respectively. This is consistent with Malhotra’s (1995) resonant capture theory that explains the orbital dynamics of Pluto and Plutinos.

If we now assume that the inner annulus (emerged from the gap formation) contained terrestrial planets and main asteroid belt, and that the asteroids between 2.1 and 3.2 AU are the remnants of secular migrations, one can fit our annular disk to the structure of the inner solar system by setting $b = \bar{a}_{\text{AST}}/a_0 = 3.81$ AU. Doing so, present orbital semi-major axes of Venus, the Earth and Mars will lie in the region affected by the density bumps of modes A_1 and A_2 (bottom panel in Figure 5). We note that the mean radial distance between the density bumps of unstable modes and the accumulation point is approximately equal to the distance from the position of maximum orbital precession (with $d\varpi_c/dR = 0$) to the position of maximum pressure. This characteristic length depends on the radial variations of surface density, sound speed and gravitational potential, but the relative positions of unstable modes and the accumulation point seems to be model-independent because the maximum precession rate occurs where the surface density is rising, and the region with maximum gas pressure is close to the region with maximum surface density.

Our theory cannot be directly applied to the formation of gas giants, Jupiter and Saturn, because the gas disk

was not responsive to perturbations in the particle phase. Nonetheless, we can make useful predictions about the possible origins of gas giants and see whether they could have interfere with the formation of rocky planets. First of all, Jupiter and Saturn lie well within the inner ring characterized by $b = 3.81$ AU, and since we have not detected any instability of the particle phase at their current orbital distances, they have probably formed from an instability in the gas phase. We compute Toomre’s Q over the inner ring and in terms of dimensionless variables:

$$Q = \frac{c_s \kappa}{\pi \Sigma_g} = \frac{\sqrt{2\pi} q}{3M_g R^{3/2}} \left[\frac{(1 + R^2)^{5/2}}{R^{19/8}} + \mathcal{O}(\mu) \right], \quad (39)$$

where $\kappa = \Omega + \mathcal{O}(\mu)$ is the epicyclic frequency of near-circular orbits. The function $Q(R)$ has a global minimum at $R_{\text{cr}} = 1.856$, and its minimum value is $Q_{\text{min}} = 3.168 q/M_g$. Near the orbit of Jupiter we have $q = 0.024$. The gas phase thus becomes unstable there if $Q_{\text{min}} < 1$ that implies $M_g > 0.076$. This corresponds to a more massive disk than minimum solar nebula and models investigated in Table 2. Nevertheless, the predicted mass threshold falls well in the mass range of circumstellar disks observed around nearby stars. The most

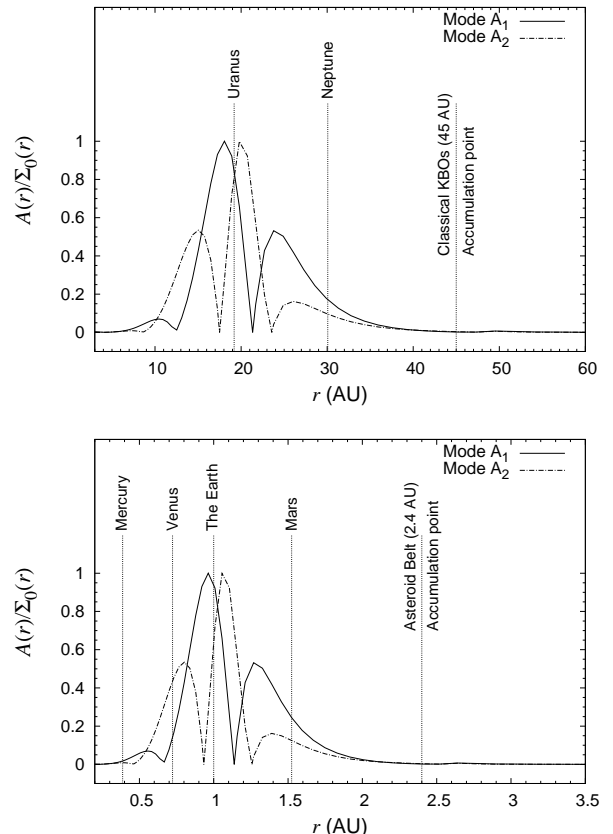


Figure 5. Normalized amplitude profiles $A(r)/\Sigma_0(r)$ of unstable modes A_1 and A_2 for model 1 in Table 2. *Top:* Classical KBOs reside at the accumulation point and we have set $b = \bar{a}_{\text{KBO}}/a_0 = 71.43$ AU. The current semi-major axes of the orbits of Saturn and Neptune are indicated by vertical dotted lines. *Bottom:* Unstable modes are fit to the inner solar system with $b = \bar{a}_{\text{AST}}/a_0 = 3.81$ AU. The mean semi-major axis of the most populous asteroid belt, and the present semi-major axes of the terrestrial planets have been indicated by vertical dotted lines.

striking point of this calculation is that when one sets $b = \bar{a}_{\text{AST}}/a_0 = 3.81$ AU, short-wavelength instabilities in the gas phase can be triggered around $r_{\text{cr}} = R_{\text{cr}}b = 7.07$ AU, which is halfway between the orbits of Jupiter and Saturn. For $M_{\text{g}} = 0.084$, equation $Q(R) - 1 = 0$ has two roots at $r_1 = 4.95$ and $r_2 = 10.6$ AU, and the entire region between the orbits of Jupiter and Saturn is unstable in Toomre's sense. Such short-wavelength instabilities will not affect inner regions where the particle phase is unstable and rocky planets are being assembled.

6. PHYSICAL RANGES OF PARAMETERS

In this section we determine over which physical ranges of parameters the perturbation solutions of the Fokker-Planck equation are acceptable. Throughout the calculations of this section, we set $M_{\star} = M_{\odot}$ and use a density of $\rho_{\text{s}} = 3 \text{ g cm}^{-3}$ for solid particles.

We have ignored particle-particle collisions in writing equation (29) and this simplification is legitimate if particles collide after several orbital periods. In a monodisperse system of spherical particles, the collisional cross section is $S_{\text{p}} = \pi(2r_{\text{p}})^2$. Moreover, the radial velocity dispersion of particles in our disks is determined from

$$\sigma_R = \langle v_R^2 \rangle^{1/2} = \sqrt{\frac{2}{\pi}} \bar{e} R \kappa, \quad (40)$$

with κ being the epicyclic frequency of near-circular orbits. In the absence of gas, the collision time t_{collide} (in the disk mid-plane) normalized to the orbital period t_{orbit} reads

$$\bar{t}_{\text{collide}} = \frac{t_{\text{collide}}}{t_{\text{orbit}}} = \frac{1}{\sqrt{2\pi}\Sigma_{\text{p}}} \left(\frac{m_{\text{p}}}{M_{\star}} \right) \left(\frac{b^2}{S_{\text{p}}} \right) \frac{h_{\text{p}}\Omega}{\sigma_R}, \quad (41)$$

where h_{p} is the scale-height of the particle disk. In low-mass disks particles can be scattered up to a vertical distance of $h_{\text{p}} = \sigma_R/\Omega + \mathcal{O}(\mu)$, and equation (41) yields

$$\bar{t}_{\text{collide}} = \frac{1}{\sqrt{2\pi}\Sigma_{\text{p}}} \left(\frac{m_{\text{p}}}{M_{\star}} \right) \left(\frac{b^2}{S_{\text{p}}} \right) + \mathcal{O}(\mu). \quad (42)$$

At $R = 0.3$, which is the position of the node of mode A₁ and the mean orbital distance of its two density bumps, we obtain

$$\bar{t}_{\text{collide}} \approx \frac{2.6}{10^4 \bar{M}_{\text{p}}} \left(\frac{r_{\text{p}}}{1 \text{ m}} \right) \left(\frac{b}{1 \text{ AU}} \right)^2, \quad (43)$$

with $\bar{M}_{\text{p}} = \mu_{\text{p}}\mu/(1 + \mu_{\text{p}})$. Since particle-particle collisions can be ignored only for $\bar{t}_{\text{collide}} \gg 1$, our governing equations are valid for all models of Table 2 and for $b = 3.81$ AU (this is the length scale of the inner solar system) if $r_{\text{p}} \gg 1.2$ m. This size threshold reduces to $r_{\text{p}} \gg 3.5$ mm by adopting $b = 71.43$ AU for the outer solar system. On the other hand, the mean free path of gas molecules is defined as (e.g., Blundell & Blundell 2006, §8.3)

$$\lambda = \frac{b}{\sqrt{2}\rho_{\text{g}}} \left(\frac{m_{\text{g}}}{M_{\star}} \right) \left(\frac{b^2}{S_{\text{g}}} \right). \quad (44)$$

Note that ρ_{g} is the dimensionless spatial density of the gas disk (see §3). For molecular hydrogen, we have $m_{\text{g}} = 3.32 \times 10^{-27}$ kg and the collision cross section is $S_{\text{g}} \approx$

$2 \times 10^{-19} \text{ m}^2$. At $R = 0.3$ and in the disk mid-plane we obtain

$$\lambda \approx \frac{2.9h}{10^3 M_{\text{g}}} \left(\frac{b}{1 \text{ AU}} \right)^3 \text{ m}. \quad (45)$$

Assuming a scale-height $h = 0.01$ (e.g., Goldreich & Ward 1973) in the models of Table 2, we find $\lambda \approx 4\text{--}16$ cm for $b = 3.81$ AU and $\lambda \approx 300\text{--}1000$ m for $b = 71.43$ AU. From the acceptable values of r_{p} for having a collisionless particle phase and the physical range of λ , we conclude that particles interact with gas molecules through Stokes drag (skin friction) if we apply our model to the inner solar system. In such a circumstance, one must use the following drag parameter

$$\xi_0 = \frac{1}{2} C_{\text{D}} \pi \left(\frac{M_{\star}}{m_{\text{p}}} \right) \left(\frac{r_{\text{p}}}{b} \right)^2, \quad (46)$$

where the drag coefficient C_{D} depends on the Reynolds number. In the outer solar system, the drag force is computed from equations (20) and (22) up to km-size objects; it then switches to Stokes drag. When particles move with supersonic speeds with the Mach number $\mathcal{M} \sim eR\Omega/c_{\text{s}} \gtrsim 3$, the drag coefficient approximately becomes $C_{\text{D}} \approx 0.92$ (Liu 1958).

Perturbation theory fails for large values of drag force, and one needs to constrain particle sizes (to which our results are applied) by the value of ξ . From equation (46) one can write

$$r_{\text{p}} = \frac{3bC_{\text{D}}}{8\sqrt{2\pi}h\xi} \left(\frac{M_{\star}}{b^3\rho_{\text{s}}} \right) \approx \frac{4410C_{\text{D}}}{h\xi} \left(\frac{1 \text{ AU}}{b} \right)^2 \text{ m}. \quad (47)$$

Consequently, the maximum value of ξ reachable by perturbation theory puts a minimum threshold on the allowed particle sizes. Our numerical experiments show that by increasing the drag parameter to $\xi_{\text{max}} \sim 1$ the accuracy of mode A₁ drops significantly and the amplitude function $A(R)$ of that mode loses its smoothness, especially for smaller fraction of solid particles. Using this empirical upper limit of ξ , and with $h = 0.01$, $C_{\text{D}} = 0.92$ and $b = 3.81$ AU, we require $r_{\text{p}} \gtrsim 28$ km to ensure the validity of perturbation theory. A nonlinear Fokker-Planck equation solver is thus needed to understand the physics of global instabilities for sub-km and km-size particles in the inner solar system. Choosing $C_{\text{D}} = 2$ (collisional/Epstein drag regime) and $b = 71.43$ AU, we obtain $r_{\text{p}} \gtrsim 170$ m, which is smaller than the mean free path of gas molecules in the outer solar system.

For the valid ranges of r_{p} discussed above, one can readily verify that the dimensionless stopping time parameter

$$\tau_{\text{s}} = \Omega t_{\text{stop}} = \sqrt{2\pi} \frac{\Omega h}{\Sigma_{\text{g}} c_{\text{s}}} \left(\frac{\rho_{\text{s}} b^3}{M_{\star}} \right) \left(\frac{r_{\text{p}}}{b} \right), \quad (48)$$

satisfies $\tau_{\text{s}} \gg 1$ in regions affected by unstable modes. The stopping time t_{stop} in equation (48) has been defined based on Epstein drag law. One still finds $\tau_{\text{s}} \gg 1$ if Stokes drag force applies. Therefore, solid particles are not dynamically coupled to the gas flow and modeling the collective dynamics of particles in the context of kinetic theory is justified.

7. DISCUSSIONS

The infall time scale of $\mathcal{O}(10^2)$ yr for meter-sized solid bodies puts a strong constraint on the formation of planetesimals from dust grains and pebbles (Weidenschilling 1977). Recent simulations have shown that the backreaction of particles on gas can trigger out-of-plane Kelvin-Helmholtz instability, which boosts local particle density and helps self-gravity to assemble km-size bodies. Turbulence, on the other hand, imposes stochastic forces on planetesimals, increases their collision frequency and disrupts those with ≤ 10 km radius (Nelson & Gressel 2010). Although the random forcing of planetesimals can be suppressed in the presence of a dead zone (Gressel et al. 2011), alternative and simpler processes may also be involved in the formation of super km-scale planetesimals.

Slow density waves exist in all near-Keplerian, self-gravitating rings and can be excited by encounters (JT12). Addition of a gas component, however, destabilizes the particle phase without any external disturbance. We showed that the drag-induced infall of solid bodies into the central star is not a universal phenomenon and the direction of particle migration highly depends on the disk structure. There will be no infall if at some region the disk density profile, including its solid particle and gas components, rises outwards. Therefore, with a preserved source of solid particles in the disk, global instabilities explored in this study will have time to boost the particle density to arbitrarily large levels and enhance the formation of bigger objects through gravitational collapse. One of the fundamental achievements of this study was how secular migrations and global instabilities can be used to identify possible planet forming regions in observed protoplanetary systems and debris disks.

Although the gas flow in our disks was in laminar regime, turbulence does not seem to considerably change our fundamental results. Youdin (2011) estimates turbulent eddy length as

$$\ell_{\text{eddy}} = \sqrt{\alpha} \frac{c_s}{\Omega} = \sqrt{\frac{\pi\alpha}{8}} q R^{9/8} + \mathcal{O}(\mu) \quad (49)$$

where α is the dimensionless turbulent diffusivity. For $\alpha \lesssim 10^{-3}$ used by Youdin (2011), we see that ℓ_{eddy} is smaller, at least by three orders of magnitude, than the scale of the wave packets (and therefore the wavelength) of unstable modes. Therefore, turbulent diffusion is unimportant in the development of global density waves and their growth.

Michikoshi et al. (2010) have also studied the formation of planetesimals through gravitational instability.

They assumed a non-responsive gas component, as we did, and introduced fluid dynamical equations to model the dynamics of dust particles in a local simulation box that rotates with Keplerian angular velocity. They then derived a dispersion relation by linearizing the continuity, momentum and Poisson equations, and showed the existence of secularly unstable long wavelength modes for a dissipative dust layer. This is somehow consistent with our findings that unstable modes have a long wavelength nature. However, their perturbation theory and N -body simulations that utilize a rotating simulation box with periodic boundary conditions, are not able to provide a global picture of particle migrations and information about possible planet forming regions. Moreover, the analytical results of Michikoshi et al. (2010) are valid only for particles dynamically coupled to gas, otherwise fluid dynamical equations with an isotropic pressure tensor could not be applied to the particle phase. Our findings apply to dispersive particle disks where the evolution of orbital eccentricity does matter.

Due to computational difficulties of working with large values of K in f_0 and a small mass ratio μ_p , we investigated global modes only for $K = 29$ that gives $\bar{e} = 0.156$. In accordance with WKB theory (JT12), decreasing the mean eccentricity of the particle disk is expected to preserve global stable modes, which then bifurcate to unstable density waves in the presence of gas drag. For smaller mean eccentricities, the number of global modes may even increase as the resonant cavities of slow modes become thinner. A useful future experiment would be to decrease \bar{e} using a Schwarzschild DF and determine the number and shape of exponentially growing modes for $\mu_p \lesssim 0.01$.

Our results have been obtained for self-gravitating disks whose particle phase is constituted from monodisperse hard spheres. Including the size distribution of particles and the effect of particle-particle collisions, especially catastrophic disruptions, is an interesting open problem. Moreover, by assuming $\Sigma_p \ll \Sigma_g$ we neglected the backreaction of particles on gas flow. A more accurate procedure is to simultaneously perturb the hydrodynamic and Fokker-Planck equations for the gas and particle phases, respectively. We anticipate angular momentum exchange between the particle and gas phases, and any particle migration should induce radial mass transfer in the gas phase.

I thank Scott Tremaine for his stimulating discussions during the course of this project. I also thank the referee for useful comments that inspired me to carry out new computations and improve the presentation of the paper.

APPENDIX

GENERALIZED FORCES IN THE ANGLE-ACTION SPACE

We define (v_R, v_ϕ) as the velocity components of particles in the polar coordinates (R, ϕ) , and the streaming velocity of the gas component will become $U_\phi(R)e_\phi$ where $U_\phi(R)$ has the functional form of $v_{g,c}$. Using the action variables $\mathbf{J} = (J_1, J_2)$ and their conjugate angles $\mathbf{w} = (w_1, w_2)$, the radial distance and azimuthal position of a test particle is calculated from

$$R = \sum_{l=-\infty}^{+\infty} \xi_l(\mathbf{J}) e^{ilw_1}, \quad e^{i\phi} = e^{iw_2} \sum_{l=-\infty}^{+\infty} \eta_l(\mathbf{J}) e^{ilw_1}, \quad (A1)$$

where the Fourier coefficients are given by

$$\xi_l(\mathbf{J}) = \frac{1}{2\pi} \oint R \cos(lw_1) dw_1, \quad \eta_l(\mathbf{J}) = \frac{1}{2\pi} \oint \cos(\phi - w_2 - lw_1) dw_1. \quad (\text{A2})$$

These integrals are taken over a full cycle of rosette orbits. From (A1) one can compute the variations δR and $\delta\phi$ as

$$\delta R = \sum_{l=-\infty}^{+\infty} \left[\imath l \xi_l e^{\imath lw_1} \delta w_1 + \frac{\partial \xi_l}{\partial J_i} \delta J_i e^{\imath lw_1} \right], \quad (\text{A3})$$

$$\delta\phi = \delta w_2 + \sum_{l,l'=-\infty}^{+\infty} \left[l \eta_l \eta_{(-l')} \delta w_1 - \imath \frac{\partial \eta_l}{\partial J_i} \eta_{(-l')} \delta J_i \right] e^{\imath(l+l')w_1}. \quad (\text{A4})$$

The virtual work of the drag force reads

$$-C_D(R)v_R \delta R - C_D(R)[J_2 - RU_\phi(R)] \delta\phi = F_{w_i} \delta w_i + F_{J_i} \delta J_i, \quad (\text{A5})$$

where $C_D(R) = \xi_0 e v_{p,c} \rho_g$ if the orbital eccentricity e satisfies the inequality $e > v_{\text{th}}/v_{p,c}$ and $C_D(R) = \xi_0 v_{\text{th}} \rho_g$ otherwise. We now utilize the following Fourier expansions

$$-C_D(R)v_R = \imath \sum_{l=-\infty}^{+\infty} Q_{R,l}(\mathbf{J}) e^{\imath lw_1}, \quad Q_{R,l}(\mathbf{J}) = \frac{1}{2\pi} \oint C_D(R)v_R \sin(lw_1) dw_1, \quad (\text{A6})$$

$$-C_D(R)[J_2 - RU_\phi(R)] = \sum_{l=-\infty}^{+\infty} Q_{\phi,l}(\mathbf{J}) e^{\imath lw_1}, \quad Q_{\phi,l}(\mathbf{J}) = -\frac{1}{2\pi} \oint C_D(R)[J_2 - RU_\phi(R)] \cos(lw_1) dw_1, \quad (\text{A7})$$

and obtain

$$F_{w_1} = - \sum_{l,l'=-\infty}^{+\infty} l' Q_{R,l} \xi_{l'} e^{\imath(l+l')w_1} + \sum_{l,l',l''=-\infty}^{+\infty} l Q_{\phi,l''} \eta_l \eta_{(-l')} e^{\imath(l+l'+l'')w_1}, \quad (\text{A8})$$

$$F_{w_2} = \sum_{l=-\infty}^{+\infty} Q_{\phi,l} e^{\imath lw_1}, \quad (\text{A9})$$

$$F_{J_i} = \sum_{l,l'=-\infty}^{+\infty} \imath Q_{R,l} \frac{\partial \xi_{l'}}{\partial J_i} e^{\imath(l+l')w_1} - \sum_{l,l',l''=-\infty}^{+\infty} \imath \frac{\partial \eta_l}{\partial J_i} \eta_{(-l')} Q_{\phi,l''} e^{\imath(l+l'+l'')w_1}, \quad i = 1, 2. \quad (\text{A10})$$

REFERENCES

- Armitage P.J., 2010, *Astrophysics of Planet Formation*, Cambridge University Press, Cambridge
 Bai X.-N., Stone J.M., 2010a, *ApJS*, 190, 297
 Bai X.-N., Stone J. M., 2010b, *ApJ*, 722, 1437
 Binney J., Tremaine S., 2008, *Galactic Dynamics*, 2nd edition, Princeton University Press, Princeton
 Blum J., Wurm G., 2008, *ARA&A*, 46, 21
 Blundell S.J., Blundell K.M., 2006, *Concepts in Thermal Physics*, Oxford University Press, New York
 Canup R.M., 2004, *ARA&A*, 42, 441
 Goldreich P., Ward W.R., 1973, *ApJ*, 183, 1051
 Gressel O., Nelson R.P., Turner N.J., 2011, *MNRAS*, 415, 3291
 Haghighipour N., Boss A.P., 2003, *ApJ*, 583, 996
 Hashimoto J. et al., 2011, *ApJ*, 729, L17
 Jalali M.A., 2007, *ApJ*, 669, 218
 Jalali M.A., 2010, *MNRAS*, 404, 1519
 Jalali M.A., Tremaine S., 2012, *MNRAS*, 421, 2368
 Johansen A., Klahr H., Henning Th., 2006, *ApJ*, 636, 1121
 Johansen A., Oishi J.S., Mac Low M.-M., Klahr H., Henning Th., Youdin A., 2007, *Nature*, 448, 1022
 Johansen A., Klahr H., Henning Th., 2011, *A&A*, 529, A62
 Kwok S., 1975, *ApJ*, 198, 583
 Liu V.C., 1958, *Journal of Applied Physics*, 29, 194
 Malhotra R., 1995, *AJ*, 110, 420
 Matsuyama I., Johnstone D., Hartmann L., 2003, *ApJ*, 582, 893
 Michikoshi S., Kokubo E., Inutsuka S.-I., 2010, *ApJ*, 719, 1021
 Nelson R. P., Gressel O., 2010, *MNRAS*, 409, 639
 Rosenbluth M.N., MacDonald W.M., Judd D.L., 1957, *Physical Review*, 107, 1
 Shu F. H., Johnstone D., Hollenbach D., 1993, *Icarus*, 106, 92
 Weidenschilling S. J., 1977, *MNRAS*, 180, 57
 Youdin A.N., Goodman J., 2005, *ApJ*, 620, 459
 Youdin A.N., 2011, *ApJ*, 731, 99